crystals

MDPI

Article

Site Occupancy Preference and Magnetic Properties in $Nd_2(Fe,Co)_{14}B$

Xubo Liu * and Ikenna C. Nlebedim

Critical Materials Innovation Hub, Division of Critical Materials, Ames National Laboratory US DOE, Ames, IA 50011, USA; nlebedim@ameslab.gov
* Correspondence: liux@ameslab.gov

Abstract: Partial replacement of Fe by Co is an effective method to increase Curie temperature (T_C), which improves the thermal stability of magnetic properties in $Nd_2Fe_{14}B$-based permanent magnets. The correlation between Fe substitution and magnetic properties has been studied in $Nd_2(Fe,Co)_{14}B$ via a first-principles calculation. The calculated Fe substitution energies indicate that the Co atoms avoid the $8j_2$ site, which agrees with the experiments. The Co atoms are ferromagnetically coupled with Fe sublattice and show magnetic moments of about 1.2 to 1.7 μ_B at different crystallographic sites, less than that of Fe (2.1–2.7 μ_B), resulting in the decrease in total magnetization at ground state (0 K) with increasing Co content. The effective exchange interaction parameter, derived from the energy difference between varied magnetic structures, increases from 7.8 meV to 17.0 meV with increasing Co content from x = 0 to x = 14 in $Nd_2Fe_{14-x}Co_xB$. This change in the effective exchange interaction parameter is responsible for the enhancement of T_C in $Nd_2(Fe,Co)_{14}B$. The total magnetization at 300 K, derived from mean-field theory, shows a peak maximum value at $x = 1$ in $Nd_2Fe_{14-x}Co_xB$. The phenomenon results from the interplay between the reduction of the magnetic moment in the Fe(Co) sublattice and the enhancement of T_C with increasing Co content.

Keywords: $Nd_2Fe_{14}B$; Nd-Fe-Co-B; substitution energy; magnetization; exchange interaction; permanent magnet; Cobalt

Citation: Liu, X.; Nlebedim, I.C. Site Occupancy Preference and Magnetic Properties in $Nd_2(Fe,Co)_{14}B$. *Crystals* **2024**, *14*, 370. https://doi.org/10.3390/cryst14040370

Academic Editor: Arcady Zhukov

Received: 22 March 2024
Revised: 8 April 2024
Accepted: 9 April 2024
Published: 16 April 2024

1. Introduction

Nd-Fe-B ($Nd_2Fe_{14}B$) permanent magnets have been widely applied in green energy fields such as wind generators and electric vehicles [1–5]. Although the Nd-Fe-B magnet is the strongest magnet at room temperature, the extrinsic magnetic properties, such as coercivity and maximum energy product, decrease rapidly above 100 °C because of its relatively low Curie temperature (T_C = 312 °C) [5,6]. One approach to enable the magnets to operate above 150 °C is to enhance magnetocrystalline anisotropy (MCA), hence the high-temperature coercivity, by the partial substitution of Nd with heavy rare earth elements (HRE) such as Dy or Tb, i.e., $(Nd_{1-x}HRE_x)_2Fe_{14}B$ (2:14:1) [3,7–12]. The strong MCA originates from the interaction between the crystal field and the spin–orbit coupling of rare earth 4*f* electrons [13,14]. The enhancement of the MCA field by Dy or Tb is related to the special 4*f* electron structure and the exchange coupling with the Fe sublattice in $Nd_2Fe_{14}B$ [14,15]. Upon the partial replacement of Nd by Dy or Tb, the coercivity can increase from about 12 kOe to 30 kOe. The replacement of Nd by Dy or Tb also reduces the saturation magnetization of the 2:14:1 phase, decreasing the maximum energy product. Further, the resource scarcity and high cost of Dy and Tb limit their application. To reduce the use of Dy and Tb in Nd-Fe-B magnet, researchers developed the grain boundary diffusion processing (GBDP) approach to enhance the coercivity [16–18]. A straightforward approach to GBDP is dip-coating DyF_3 or TbF_3 on the surface of the Nd-Fe-B magnet plus the subsequent heat treatment above the Nd-rich grain boundary phase (GBP) melting point [18]. In GBDP-treated NdFeB magnet, the Dy or Tb-rich layer on the 2:14:1 surface

suppresses the nucleation of the reverse magnetic domain during the demagnetization process, enhancing the coercivity [18]. The partial replacement of Nd by Dy or Tb can effectively increase the absolute value of coercivity, but the temperature coefficients of coercivity (i.e., the rate of decrease with temperature) are still high. A small amount of Co is often added to improve the T_C and enhance the thermal stability of magnetic properties in Nd-Fe-B [6,19]. The partial replacement of Fe by Co will reduce the temperature coefficient of magnetic remanence and coercivity. However, the absolute value of MCA also decreases with increasing Co content. In high-performance Nd-Fe-B magnet manufacturing, both Co and Dy or Tb are used to maximize the performance. In addition, some elements, such as Al, Si, Ga, and Cu, have limited solubility in the 2:14:1 phase but will modify the Nd-rich grain boundary phase (GBP) to enhance coercivity [20–23].

Since the Nd-Fe-B magnet's discovery, much research has been conducted on the elemental substitutions in $Nd_2Fe_{14}B$ [6,19]. One interesting phenomenon is that the Fe substitution by other elements in $Nd_2Fe_{14}B$ shows strong site preferences that are intimately related to the changes in magnetic properties. To determine the element substitution scheme in 2:14:1 and its effect on magnetic properties, scientists can perform experiments such as neutron diffraction, Mössbauer spectroscopy, and magnetic measurements. For example, Moze et al. reported that chromium and manganese are preferred substitutes for iron at the $8j_2$ sites in $Y_2Fe_{14}B$ [24]. The remaining Fe sites have a fractional occupation of Mn or Cr at a concentration below the overall stoichiometry. Neutron diffraction has been used to show that Co avoids the $8j_2$ site and slightly favors the 4*e* site in 2:14:1 [25]. van Noort and Buschow [26] found that Fe atoms strongly prefer occupying the $8j_2$ and $16k_2$ sites from Mössbauer spectroscopy. Similarly, using Mössbauer spectroscopy, Ryan et al. [27] concluded that Fe prefers the $8j_2$ sites, the other sites being randomly occupied by Co in $Nd_2Fe_{14-x}Co_xB$. Eslava et al. reported that the Co occupancy preference depends on the Co content in $Nd_2Fe_{14-x}Co_xB$ [28]. Despite these labor-, time-, and cost-intensive experimental approaches, the first-principles DFT (density function theory) calculations can predict the site occupancy and its effect on magnetic properties in intermetallic compounds such as the 2:14:1 system. It was reported [29–31] that the predictions from DFT calculations agree well with the experiments for the Fe substitution scheme in $Nd_2(Fe, M)_{14}B$ with M = Al, Si, Ga, etc.

$Nd_2Fe_{14-x}Co_xB$ forms solid solutions in all the compositional ranges [32,33]. Theoretically, understanding the role of doping Co into the 2:14:1 system at the atomic level can help develop high-performance Nd-Fe-B magnets. The knowledge gained from the 2:14:1 system and the methods developed can be applied to study other novel rare earth (RE) transition metal magnets, such as $Sm(Fe, Co, Ti)_{12}$ with a tetragonal $ThMn_{12}$ type structure [34–36]. In this work, we studied the role of Co in $Nd_2(Fe,Co)_{14}B$ from the first principle DFT calculations. We report the Co and Fe occupancy schemes at different crystallographic sites and their effect on magnetic properties in $Nd_2(Fe,Co)_{14}B$. The magnetization of $Nd_2Fe_{14-x}Co_xB$ at the finite temperature was also derived from the DFT calculation and mean-field theory.

2. Method and Computational Details

The substitution energy of the Co atom in $Nd_2(Fe,Co)_{14}B$ (E_{sub}) is calculated as the change in the cohesive energy of $Nd_2(Fe,Co)_{14}B$ to $Nd_2Fe_{14}B$. E_{sub} is derived from the DFT total energy calculations. In the calculation, the unit cell size and atomic position are relaxed. The calculation details of E_{sub} were reported previously [37]. Here, we perform the DFT modeling using a linear combination of pseudo-atomic orbital (LCPAO) methods implemented in OpenMX code [38,39]. Exchange and correlation effects are approximated with a generalized gradient approximation (GGA) given by Perdew et al. [40]. The relativistic effects are included by solving a scalar relativistic wave equation. Due to the strong on-site correlation effects, the Nd 4*f* electrons are localized as atomic-like states [41]. The 4*f* electrons of Nd are treated as an open-core state in the calculation. The open core pseudopotential is generated by assuming that the 4*f*-states are part of the core states. The

basis sets are *s*3*p*2*d*1*f*1, *s*3*p*2*d*1, *s*2*p*2*d*1, and *s*3*p*2*d*1 for Nd, Fe, B, and Co with cutoff radii of 8.0, 6.0, 7.0, and 6.0 atomic units (a.u.), respectively.

Following Hund's rules, the atomic magnetic moment of Nd, from the 4*f* electrons, is 3.27 μ_B [42]. The contribution of Nd 4*f* electrons is taken as 3.27 μ_B for the total magnetic moment calculation. The Nd 5*d*, 6*s*, and 6*p* contribution is directly derived from the DFT calculation. The calculated orbital moments of Fe and Co are small, ranging from about 0.03 to 0.1 μ_B.

Based on the Maxwell–Boltzmann distribution [43], the occupation probability of Co at each Fe site in $Nd_2(Fe,Co)_{14}B$ can be expressed as

$$P_i = \frac{g_i \exp\left(-\frac{\Delta E_i}{k_B T}\right)}{\sum_i g_i \exp\left(-\frac{\Delta E_i}{k_B T}\right)} \quad (1)$$

where g_i, ΔE_i, T, and k_B are the multiplicity of the crystallographic site i, internal energy change (i.e., E_{sub}), temperature, and Boltzmann's constant, respectively.

To mimic the random distribution of Co at a specific crystallographic site of Fe, we adopt a virtual crystal approximation (VCA), implemented in the Questaal, which is an all-electron full-potential Linear Muffin-Tin Orbital (LMTO) DFT code [44,45]. Again, the Nd 4*f* electrons are treated as open-core states in the DFT calculation. The *k*-space integrations were performed with the tetrahedron method [46,47]. The effective exchange interaction parameters of $Nd_2(Fe,Co)_{14}B$ are derived from the energy difference between the different magnetic structures of 2:14:1. The Curie temperature is estimated from the calculated effective exchange parameter based on Weiss molecular field model and Brillouin theory—the first mean-field theory for the magnetic transition [42,48]. The magnetization at finite temperature is also calculated based on the general Brillouin theory of localized magnetic moments system (i.e., mean-field theory). The temperature dependence of magnetization is described using a Brillouin function [42].

3. Results and Discussion

3.1. Substitution Energy and Site Preference of Co in $Nd_2(Fe,Co)_{14}B$

$Nd_2Fe_{14}B$ crystallizes in a tetragonal structure with a space group $P4_2/mnm$. In the unit cell, there are four formula units of $Nd_2Fe_{14}B$, i.e., 68 atoms ($Nd_8Fe_{56}B_4$). To evaluate the effect of the Fe substitution by Co in Fe-rich $Nd_2(Fe,Co)_{14}B$ compound, one Co atom is doped at a specific Fe site in a single unit cell of 2:14:1. In other words, it has a nominal composition of $Nd_2Fe_{13.75}Co_{0.25}B$ or 1.7% of Fe replaced with Co in the super-cell. Since 2:14:1 has six crystallographically inequivalent Fe sites in the unit cell, there are six geometrically different patterns for doping Co into the unit cell. Similarly, to understand the site occupancy scheme of Fe in Co-rich $Nd_2(Fe,Co)_{14}B$ phase, one Fe atom is set at a specific Co site in the 2:14:1 unit cell, i.e., a nominal composition of $Nd_2Co_{13.75}Fe_{0.25}B$.

The calculated lattice constants of $Nd_2Fe_{14}B$ (a = 8.7764 Å, c = 12.1640 Å) are comparable to the experimental values (a = 8.8 Å, c = 12.2 Å) [6]. The difference in the calculated lattice constants between $Nd_2Fe_{14}B$ and $Nd_2Fe_{13.75}Co_{0.25}B$ is less than 0.02 Å. The results indicate that a small substitution of Fe content with Co (1.7%) has almost no effect on the lattice constants in 2:14:1. As shown in Table 1, the E_{sub} values for Co are positive at the 8j_2 site (0.16 eV/atom). At the same time, the values are negative at all other Fe sites in $Nd_2Fe_{13.75}Co_{0.25}B$. The results reveal that the Co atoms prefer to avoid the 8j_2 site in Fe-rich $Nd_2(Fe,Co)_{14}B$ phase. E_{sub} has a relatively lower value at the 8j_1 site (comparable with the 4*c* site), implying a moderate occupation preference of Co at those sites in $Nd_2Fe_{13.75}Co_{0.25}B$. On the other hand, the E_{sub} values for Fe are negative at all the six Co crystallographic sites in $Nd_2Co_{13.75}Fe_{0.25}B$. E_{sub} has the lowest value at the 8j_2 site (−0.40 eV) but the highest value at the 4*e* site (−0.13 eV) in $Nd_2Co_{13.75}Fe_{0.25}B$. This indicates that in the Co-rich $Nd_2(Fe,Co)_{14}B$ phase, Fe prefers to enter the 8j_2 site and has the least preference for the 4*e* site. The result agrees with the experimental reports that in $Nd_2(Fe,Co)_{14}B$, Co and Fe prefer to avoid and occupy the 8j_2 site, respectively [25–28].

Table 1. Substitution energy E_{sub} (eV/atom per unit cell) of Fe and Co sites in $Nd_2Fe_{13.75}Co_{0.25}B$ and $Nd_2Co_{13.75}Fe_{0.25}B$, respectively. The nearest neighbors (NN) and the Wigner–Seitz volume (WSV, Å^3) of each Fe crystallographic site in $Nd_2Fe_{14}B$ are also listed.

	Co ($Nd_2Fe_{13.75}Co_{0.25}B$)	**Fe ($Nd_2Co_{13.75}Fe_{0.25}B$)**	**NN**	**WSV**
$Esub(16k_1)$	−0.10	−0.17	2Nd, 1B, 10Fe	11.9
$Esub(16k_2)$	−0.19	−0.15	2Nd, 10Fe	11.6
$Esub(8j_1)$	−0.30	−0.20	3Nd, 9Fe	12.4
$Esub(8j_2)$	0.16	−0.40	2Nd, 12Fe	12.8
$E_{sub}(4e)$	−0.04	−0.13	2Nd, 2B, 9Fe	12.1
$E_{sub}(4c)$	−0.24	−0.30	4Nd, 8Fe	12.3

The phase stability of the 2:14:1 system is less affected by doping with Co. The difference of the calculated cohesive energy between $Nd_2Fe_{14}B$ and $Nd_2Fe_{13.75}Co_{0.25}B$ is about 0.6–4.4 meV/atom, comparable to 7–50 K thermal energy. This small thermal energy has almost no effect on the phase stability of $Nd_2Fe_{14}B$, which has a melting point of 1433 K [49]. This agrees with the fact that $Nd_2Fe_{14-x}Co_xB$ forms solid solutions across the entire compositional range [33]. The E_{sub} values and signs depend on the volume of a specific crystallographic site and structural and chemical environments. We calculated the Wigner–Seitz volume and listed the neighboring atoms of the six different crystallographic Fe sites using the software DIDO95 [50]. As shown in Table 1, the $8j_2$ site has the largest site volume (12.8 Å^3). The metallic atomic radii are 1.26 Å and 1.25 Å for Fe and Co, respectively [51]. To reduce the local strain and lower the E_{sub} value, the small-sized Co atoms avoid the $8j_2$ site, while large-sized Fe atoms prefer to enter the $8j_2$ site. The distribution of Fe and Co at other sites is not completely random, as the values of E_{sub} vary from site to site. For example, the E_{sub} values for Co at the $8j_1$ site is much lower than that at the other sites in $Nd_2Fe_{13.75}Co_{0.25}B$. In addition to the different site volumes, the chemical environment varies from site to site. For example, the 4*c* site has many Nd (four Nd atoms) neighbors, while the 4*e* site has more boron nearest neighbors (three boron atoms). The magnitude of E_{sub} depends on the interplay between the volume and the chemical affinity effects.

The site occupancy preferences of Fe and Co also depend on temperature. Figure 1a displays the temperature dependence of the site occupancy of Co in $Nd_2Fe_{13.75}Co_{0.25}B$ over the six Fe(Co) crystallographic sites. The Co atoms prefer to enter the $8j_1$ site but avoid the $8j_2$ site. With increasing temperature, the occupancy fraction of Co at the $8j_1$ site decreases slightly while the occupancies of Co atoms at other sites increase (Figure 1a), which is driven by thermal energy. To highlight the site occupancy preferences, we normalize them to those expected for random distribution, which can be expressed as

$$Relat.P_i = \frac{56\ \exp(-\Delta E_i/k_BT)}{\sum_i g_i \exp(-\Delta E/k_BT)} \quad (2)$$

The difference between Formulas (1) and (2) is the normalization factor $g_i/56$, where g_i is the multiplicity of the crystallographic site *i*, and the total number of Fe(Co) atoms is 56 in the unit cell. Following this normalization, the relative occupancy P_i will be 1 for a random distribution. If the Co atom strongly prefers a specific crystallographic site *i*, the relative occupancy P_i will be much higher than 1. Similarly, the value will be much lower than one if the Co atom prefers to avoid the site. A similar method was applied to analyze the site occupancy preference from neutron diffraction data in the 2:14:1 system [28]. As shown in Figure 1b, the relative occupancy P_i for the $8j_1$ site has the largest value (2.8 at 1400 K), while that at the $8j_2$ site has the lowest value (0.03 at 1400 K). The results highlight that the Co atoms prefer the $8j_1$ site and avoid the $8j_2$ site in $Nd_2Fe_{13.75}Co_{0.25}B$. Co also has a moderate preference for the 4*c* site. These results are in good agreement with the experiments [28].

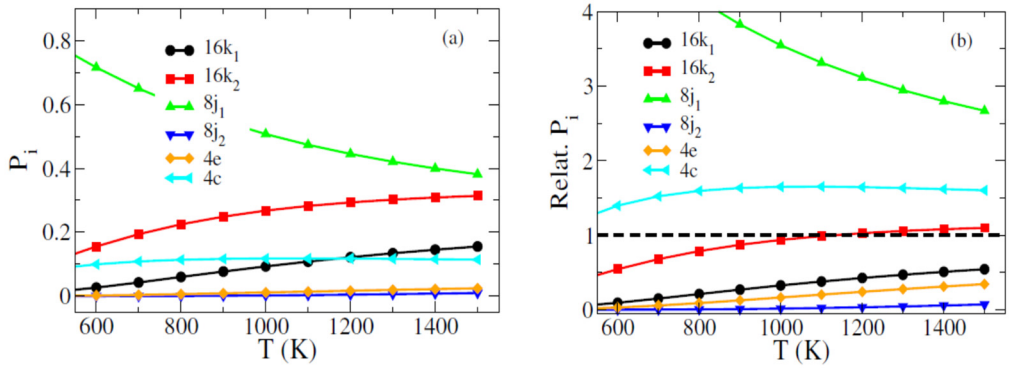

Figure 1. (Online color) Temperature dependence of the site occupancy fraction (**a**) and the normalized relative occupancy (**b**) of Co in $Nd_2Fe_{13.75}Co_{0.25}B$.

Figure 2 displays the temperature dependence of the site occupancy of Fe in $Nd_2Co_{13.75}Fe_{0.25}B$. Fe strongly prefers to enter the 8j_2 site due to its larger atomic size. Interestingly, Fe has a moderate preference at the 4*c* site in Co-rich $Nd_2(Fe,Co)_{14}B$. As discussed above, Co also moderately prefers to occupy the 4*c* site in the Fe-rich $Nd_2(Fe,Co)_{14}B$. One possible explanation is that the Fe(Co) at the 4*c* site is preferred to the neighbors of Co(Fe) as the mixing heating of Fe-Co is lower than Fe-Fe and Co-Co alloys based on the Miedema model [52]. The results indicated that the Co(Fe) occupancy scheme is sensitive to the composition of $Nd_2Fe_{14-x}Co_xB$.

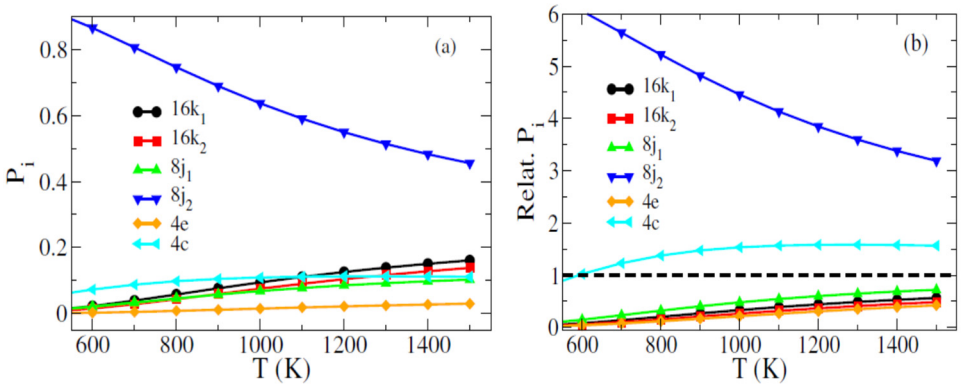

Figure 2. (Online color) Temperature dependence of the site occupancy fraction (**a**) and the normalized relative occupancy (**b**) of Fe in $Nd_2Co_{13.75}Fe_{0.25}B$.

3.2. Atomic Resolved Magnetic Moments in $Nd_2(Fe,Co)_{14}B$

Fe (Co) atoms exhibit different magnetic moments depending on the specific crystallographic site. Table 2 shows the atomic magnetic moments of Co and Fe at various crystallographic sites in $Nd_2Fe_{13.75}Co_{0.25}B$. The Co atoms show positive magnetic moments and are ferromagnetically coupled with the Fe sublattice. The Co magnetic moments range from 1.23 to 1.70 μ_B (Table 2). Cobalt has the smallest magnetic moment of 1.23 μ_B at the 4*e* site and the largest magnetic moment of 1.7 μ_B at the 8j_2 site. Similarly, Fe has the largest (2.68 μ_B) and the smallest (2.11 μ_B) magnetic moments at the 8j_2 and 4*e* sites, respectively. This behavior is ascribed to the largest site volume of the 8j_2 site (12.8 Å^3) and the largest amount of boron nearest neighbor of the 4*e* site in 2:14:1. As the magnetic moment of Co is much less than that of Fe, it is expected that the magnetization of $Nd_2Fe_{14-x}Co_xB$ would decrease with Co content.

Table 2. The atomic magnetic moments m (μ_B) of Co and Fe at different crystallographic sites in $Nd_2Fe_{13.75}Co_{0.25}B$.

	16k_1	**16k_2**	**8j_1**	**8j_2**	**4e**	**4c**
Fe	2.30	2.37	2.31	2.68	2.11	2.48
Co	1.37	1.48	1.42	1.70	1.23	1.53

Table 3 displays the site-resolved magnetic moments in $Nd_2Fe_{14-x}CoxB$. For x = 0.25 and 13.75, we assume that Co and Fe occupy 8j_1 and 8j_2 sites, respectively. The reason is that Co at the 8j_1 site and Fe at the 8j_2 site have their respective minimum E_{sub} values at x = 0.25 and x = 13.75. It should be noted that the crystallographic symmetry of the unit cell is reduced, and each site will be split into several sub-sites upon doping Co(Fe) in the unit cell. To facilitate the comparison, we use the original site notations and list the average magnetic moment for each site. As expected, the partial replacement of Fe by Co reduces the site-resolved magnetic moment while having little effect on the magnetic moment at other sites. Again, the atoms of Fe or Co have the largest atomic magnetic moment at the 8j_2 site. The magnitude of magnetic moment at the different site decreases following the order from 8j_2 to 4c, 16k_2, 8j_1, 16k_1, and 4e.

Table 3. Site-resolved magnetic moments of M (μ_B) at different sites in $Nd_2Fe_{14-x}Co_xB$.

Site	**x = 0**	**x = 0.25 (Co@8j$_1$)**	**x = 13.75 (Fe@8j$_2$)**	**x = 14**
16k_1	2.29	2.29	1.23	1.23
16k_2	2.36	2.36	1.45	1.45
8j_1	2.30	2.18	1.51	1.51
8j_2	2.68	2.68	1.71	1.57
4e	2.11	2.12	1.05	1.06
4c	2.48	2.48	1.60	1.60

3.3. Exchange Interaction and Curie Temperature in $Nd_2(Fe,Co)_{14}B$

The partial substitution of Fe by Co effectively enhances T_C in $Nd_2(Fe,Co)_{14}B$. To understand the mechanism of the enhancement of T_C induced by doping Co, we estimate the effective exchange interaction parameter in the 2:14:1 system by comparing the energy difference between different magnetic ordering structures. Figure 3 displays a ferromagnetic (FM) structure (a) and an antiferromagnetic (AFM) structure (b) of 2:14:1, which is created using the VESTA package [53]. According to the Heisenberg model, the exchange interaction parameter, J, can be expressed as [42]

$$H = -J\widehat{S_1}.\widehat{S_2} \tag{3}$$

where S_1 and S_2 are dimensionless unit spin operators, and H is the Heisenberg Hamiltonian. The effective value of J can be estimated as follows:

$$J = -\frac{1}{2n^2}(E_{AFM} - E_{FM}) \tag{4}$$

where n, E_{AFM}, and E_{FM} are the average number of Bohr magnetons for each magnetic atom and the total energy for the AFM and FM structure, respectively.

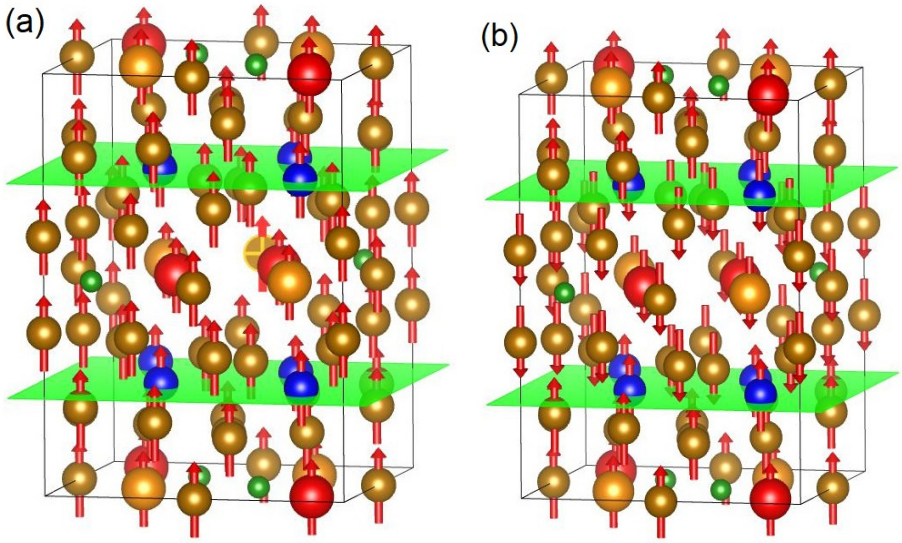

Figure 3. Unit cell of 2:14:1 with a ferromagnetic (FM) structure (**a**) and an antiferromagnetic (AFM) structure (**b**). The large red and light gold balls represent Nd atoms at 4*f* and 4*g*, respectively. The small green ball is for B. The moderate-sized blue and deep gold balls are for Fe(Co) at the $8j_2$ and the other sites, respectively. The arrows represent the magnetic moment direction of each magnetic atom. The green area highlights the position of the crystal plane with Fe(Co) $8j_2$ atoms perpendicular to the *c*-axis. All the images are generated using the VESTA package [53].

As discussed above, Co atoms prefer to avoid the $8j_2$ site in $Nd_2(Fe,Co)_{14}B$. We ignore the small preferential occupancy over other Fe(Co) crystallographic sites and assume a random distribution of Co at the other five sites, i.e., $16k_1$, $16k_2$, $8j_1$, 4*e*, and 4*c*. To mimic the partial replacement of Fe by Co, we adopt a VCA approach in DFT calculation [41]. The magnetization and total energies for the FM and AFM structures were calculated using a full-potential LMTO method as a function of Co content. More details are described in the Method and Computational Details section above.

Figure 4a shows the Co content dependence of the average magnetic moment of Fe(Co) atoms in $Nd_2Fe_{14-x}Co_xB$. The average magnetic moment slightly decreases with increasing Co content for $x < 3$. Any further increase in the Co content decreases the magnetic moment almost linearly. The effective exchange interaction parameter *J* was derived based on Equation (3) and is shown in Figure 4b. The values of *J* increase almost linearly from 7.8 meV at x = 0 to 17.0 meV at x = 16, in agreement with the fact that T_C can be substantially enhanced by doping Co in the 2:14:1 phase [6].

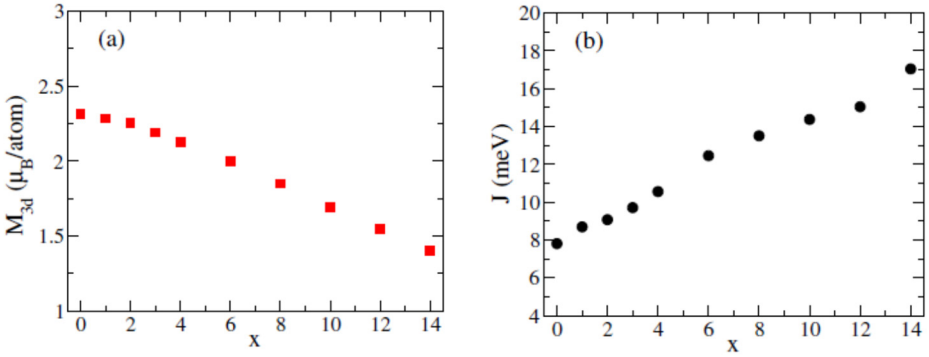

Figure 4. Calculated average magnetic moment of Fe(Co) atoms (**a**) and effective exchange interaction parameter (**b**) as a function of Co content in $Nd_2Fe_{14-x}Co_xB$.

The Curie temperature was also estimated using the calculated effective exchange interaction parameter *J*. The 2:14:1 system has two magnetic sublattices: Nd- and Fe(Co)-

sublattice. The exchange interaction in the Fe(Co) sublattice is much stronger than that of the Nd sublattice and the inter-lattice exchange interaction between Nd and Fe(Co) [6]. The Fe(Co) sublattice mainly determines T_C. We estimate T_C in $Nd_2Fe_{14-x}Co_xB$ based on the mean-field theory [42,48].

$$T_c = \frac{2ZJ}{3k_B} \quad (5)$$

where T_C, Z, J, and k_B are Curie temperature, the average number of the nearest neighbor of magnetic atoms, and Boltzmann's constant, respectively. Here, Z is taken as 12 (see Table 1).

As shown in Figure 5, the calculated T_C values increase with Co content in qualitative agreement with the experimental results [25,32]. The mechanism responsible for the concomitant increase in T_C with Co content is the enhancement of the effective exchange interaction parameter. The results imply that a mean-field model can successfully estimate the Curie temperature of rare earth Fe (Co) intermetallic compounds. This was confirmed in many other rare earth-3*d* transition metal compounds [54,55].

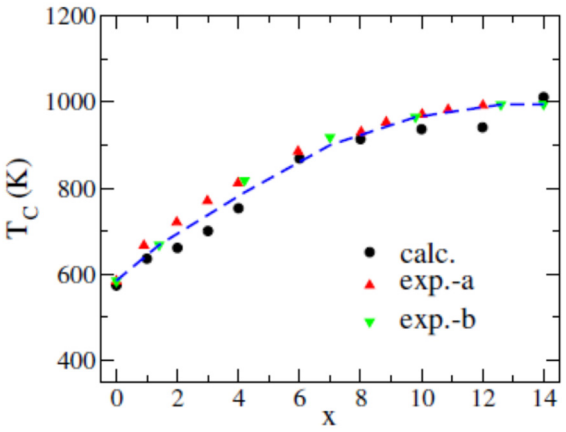

Figure 5. Calculated Curie temperature T_C (solid circle) as a function of Co content in $Nd_2Fe_{14-x}Co_xB$. The experimental values of T_C [25,32] are also plotted (up- and down-triangle). The blue dotted line is only as a guide for eyes.

3.4. Magnetization of $Nd_2(Fe,Co)_{14}B$ at Finite Temperature

The measured saturation magnetization displays a maximum at x = 1–2 in $Nd_2Fe_{14-x}Co_xB$ at 77 K and 293 K. However, the maximum is less pronounced at low temperatures [32]. In our calculations, the magnetization at the ground state continuously decreases with increasing Co content (Figure 6). To understand the peak value of saturation magnetization at finite temperature, we calculated the temperature dependence of magnetization based on the general Brillouin theory of localized magnetic moments (i.e., a mean-field theory), which is expressed using a Brillouin function B_J with $J = 1/2$ [42].

$$M(T) = M_S B_{1/2};\ B_{1/2} = 2\coth(2x) - \coth(x);\ x = M(T)\cdot T_C/T \quad (6)$$

The calculated magnetization at 300 K was also plotted as a function of Co content in Figure 6. It displays a peak value round x = 1, which is qualitatively in agreement with the experiments [33]. The formation of a weak maximum of total magnetization results from the interplay between the reduction of magnetic moment and the sharp increase in T_C in $Nd_2Fe_{14-x}Co_xB$.

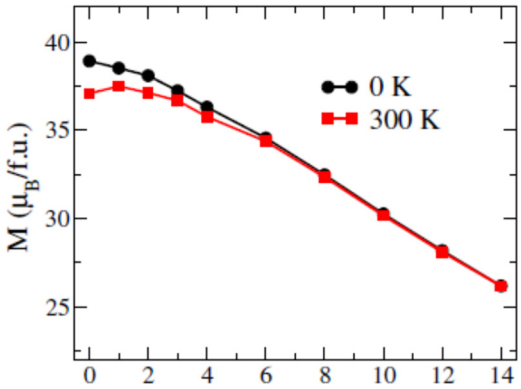

Figure 6. Calculated magnetization in $Nd_2Fe_{14-x}Co_xB$ at ground state (0 K) and 300 K.

4. Summary

The Fe and Co substitution scheme in $Nd_2(Fe,Co)_{14}B$ depends on the Co content from the DFT calculations. The calculated substitution energies indicate that the Co atoms avoid the $8j_2$ site. In addition, Co atoms prefer the $8j_1$ and 4*c* sites in $Nd_2Fe_{13.75}Co_{0.25}B$, while Fe atoms prefer the $8j_2$ and 4*c* sites in $Nd_2Co_{13.75}Fe_{0.25}B$. The Co atoms show magnetic moments of about 1.2 to 1.7 μ_B at different crystallographic sites, less than Fe (2.1–2.7 μ_B). Increasing Co content reduces total magnetization at the ground state (0 K). The effective exchange interaction parameter is also enhanced from 7.8 meV to 17.0 meV with increasing Co content from x = 0 to 14, which is responsible for the T_C enhancement in $Nd_2(Fe,Co)_{14}B$. The calculated total magnetization at 300 K shows a peak value at $x = 1$ in $Nd_2Fe_{14-x}Co_xB$. This is ascribed to the interplay between the reduced magnetic moment of the Fe(Co) sublattice and the T_C enhancement with increasing Co content.

Author Contributions: Conceptualization, X.L. and I.C.N.; methodology, X.L. and I.C.N.; software, X.L.; validation, X.L. and I.C.N.; formal analysis, X.L. and I.C.N.; investigation, X.L.; resources, I.C.N.; data curation, X.L.; writing—original draft preparation, X.L.; writing—review and editing, I.C.N.; visualization, X.L.; supervision, I.C.N.; project administration, X.L. and I.C.N.; funding acquisition, I.C.N. All authors have read and agreed to the published version of the manuscript.

Funding: This research was funded by the Critical Materials Innovation Hub funded by the U.S. Department of Energy, Office of Energy Efficiency and Renewable Energy, Advanced Materials and Manufacturing Technologies Office (AMMTO). The work was performed in Ames National Laboratory, operated for the U.S. Department of Energy by Iowa State University of Science and Technology under Contract No. DE-AC02-07CH11358.

Data Availability Statement: The data presented in this study are available on request from the corresponding author due to legal.

Conflicts of Interest: The authors declare no conflict of interest.

References

1. Sagawa, M.; Fujimura, S.; Togawa, N.; Yamamoto, H.; Matsuura, Y. New Material for Permanent Magnets on a Base of Nd and Fe (Invited). *J. Appl. Phys.* **1984**, *55*, 2083–2087. [CrossRef]
2. Croat, J.J.; Herbst, J.F.; Lee, R.W.; Pinkerton, F.E. Pr-Fe and Nd-Fe-Based Materials: A New Class of High-Performance Permanent Magnets (Invited). *J. Appl. Phys.* **1984**, *55*, 2078–2082. [CrossRef]
3. Sugimoto, S. Current Status and Recent Topics of Rare-Earth Permanent Magnets. *J. Phys. D Appl. Phys.* **2011**, *44*, 064001. [CrossRef]
4. McCallum, R.W.; Lewis, L.; Skomski, R.; Kramer, M.J.; Anderson, I.E. Practical Aspects of Modern and Future Permanent Magnets. *Annu. Rev. Mater. Res.* **2014**, *44*, 451–477. [CrossRef]
5. Gutfleisch, O.; Willard, M.A.; Brück, E.; Chen, C.H.; Sankar, S.G.; Liu, J.P. Magnetic Materials and Devices for the 21st Century: Stronger, Lighter, and More Energy Efficient. *Adv. Mater.* **2011**, *23*, 821–842. [CrossRef]
6. Herbst, J.F. $R_2Fe_{14}B$ Materials: Intrinsic Properties and Technological Aspects. *Rev. Mod. Phys.* **1991**, *63*, 819–898. [CrossRef]
7. Sepehri-Amin, H.; Ohkubo, T.; Hono, K. Grain Boundary Structure and Chemistry of Dy-Diffusion Processed Nd–Fe–B Sintered Magnets. *J. Appl. Phys.* **2010**, *107*, 09A745. [CrossRef]

8. Gabay, A.M.; Marinescu, M.; Li, W.F.; Liu, J.F.; Hadjipanayis, G.C. Dysprosium-Saving Improvement of Coercivity in Nd-Fe-B Sintered Magnets by Dy_2S_3 Additions. *J. Appl. Phys.* **2011**, *109*. [CrossRef]
9. Yue, M.; Liu, W.Q.; Zhang, D.T.; Jian, Z.G.; Cao, A.L.; Zhang, J.X. Tb Nanoparticles Doped Nd-Fe-B Sintered Permanent Magnet with Enhanced Coercivity. *Appl. Phys. Lett.* **2009**, *94*, 092501. [CrossRef]
10. Cao, X.; Chen, L.; Guo, S.; Chen, R.; Yan, G.; Yan, A. Magnetic and Microstructural Properties of DyF3-Coated Sintered Nd-Fe-B Magnets by Electrophoretic Deposition. *IEEE Trans. Magn.* **2015**, *51*, 2101804. [CrossRef]
11. Liu, X.; Wang, X.; Liang, L.; Zhang, P.; Jin, J.; Zhang, Y.; Ma, T.; Yan, M. Rapid Coercivity Increment of Nd-Fe-B Sintered Magnets by $Dy_{69}Ni_{31}$ Grain Boundary Restructuring. *J. Magn. Magn. Mater.* **2014**, *370*, 76–80. [CrossRef]
12. Liu, X.B.; Altounian, Z. The Partitioning of Dy and Tb in NdFeB Magnets: A First-Principles Study. *J. Appl. Phys.* **2012**, *111*, 07A701. [CrossRef]
13. Yosida, K.; Okiji, K.; Chikazumi, S. Magnetic Anisotropy of Localized State in Metals. *Prog. Theor. Phys.* **1965**, *33*, 559. [CrossRef]
14. Delange, P.; Biermann, S.; Miyake, T.; Pourovskii, L. Crystal-Field Splittings in Rare-Earth-Based Hard Magnets: An Ab Initio Approach. *Phys. Rev. B* **2017**, *96*, 155132. [CrossRef]
15. Gimaev, R.; Komlev, A.; Davydov, A.; Kovalev, B.; Zverev, V. Magnetic and Electronic Properties of Heavy Lanthanides (Gd, Tb, Dy, Er, Ho, Tm). *Crystals* **2021**, *11*, 82. [CrossRef]
16. Lv, M.; Kong, T.; Zhang, W.; Zhu, M.; Jin, H.; Li, W.; Li, Y. Progress on Modification of Microstructures and Magnetic Properties of Nd-Fe-B Magnets by the Grain Boundary Diffusion Engineering. *J. Magn. Magn. Mater.* **2021**, *517*, 167278. [CrossRef]
17. Chen, F. Recent Progress of Grain Boundary Diffusion Process of Nd-Fe-B Magnets. *J. Magn. Magn. Mater.* **2020**, *514*, 167227. [CrossRef]
18. Liu, Z.; He, J.; Ramanujan, R.V. Significant Progress of Grain Boundary Diffusion Process for Cost-Effective Rare Earth Permanent Magnets: A Review. *Mater. Des.* **2021**, *209*, 110004. [CrossRef]
19. Burzo, E. Permanent Magnets Based on R-Fe-B and R-Fe-C Alloys. *Rep. Prog. Phys.* **1998**, *61*, 1099–1266. [CrossRef]
20. Li, W.F.; Ohkubo, T.; Akiya, T.; Kato, H.; Hono, K. The Role of Cu Addition in the Coercivity Enhancement of Sintered Nd-Fe-B Permanent Magnets. *J. Mater. Res.* **2009**, *24*, 413–420. [CrossRef]
21. Liu, X.B.; Altounian, Z. The Role of Cu in Sintered Nd-Fe-b Magnets: Ab Initio Study. *IEEE Trans. Magn.* **2012**, *48*, 3144–3146. [CrossRef]
22. Sepehri-Amin, H.; Li, W.F.; Ohkubo, T.; Nishiuchi, T.; Hirosawa, S.; Hono, K. Effect of Ga Addition on the Microstructure and Magnetic Properties of Hydrogenation-Disproportionation-Desorption-Recombination Processed Nd-Fe-B Powder. *Acta Mater.* **2010**, *58*, 1309–1316. [CrossRef]
23. Liu, Y.; He, J.; Yu, H.; Liu, Z.; Zhang, G. Restoring and Enhancing the Coercivity of Waste Sintered (Nd,Ce,Gd)FeB Magnets by Direct Pr–Tb–Cu Grain Boundary Diffusion. *Appl. Phys. A* **2020**, *126*, 657. [CrossRef]
24. Moze, O.; Pareti, L.; Solzi, M.; Bolzoni, F.; David, W.I.F.; Harrison, W.T.A.; Hewat, A.W. Magnetic Structure and Preferential Site Occupation in Manganese- and Chromium-Substituted Y2Fe14B Compounds. *J. Less Common Met.* **1988**, *136*, 375–383. [CrossRef]
25. Herbst, J.F.; Yelon, W.B. Preferential Site Occupation and Magnetic Structure of $Nd_2(Co_xFe_{1-x})$ 14B Systems. *J. Appl. Phys.* **1986**, *60*, 4224–4229. [CrossRef]
26. van Noort, H.M.; Buschow, K.H.J. On the Site Preference of 3d Atoms in Compounds of the $R_2(Co_{1-x}Fe_x)$14B Type. *J. Less Common Met.* **1985**, *113*, L9–L12. [CrossRef]
27. Ryan, D.H.; Altounian, Z.; Liao, L.X.; Ström-Olsen, J.O.; Muir, W.B. Direct Determination of Cobalt Site Preferences at Infinite Dilution in Iron-Based Intermetallic Compounds (Invited). *J. Appl. Phys.* **1990**, *67*, 4742–4746. [CrossRef]
28. Eslava, G.G.; Ito, M.; Colin, C.V.; Yano, M.; Shoji, T.; Kato, A.; Suard, E.; Dempsey, N.M.; Givord, D. Preferential Co and Fe Atom Occupancy in $R_2(Fe_{1-X}Co)_{14}B$ Intermetallic Compounds (R = Nd, Y and Ce). *J. Alloys Compd.* **2021**, *851*, 156168. [CrossRef]
29. Liu, X.B.; Ma, Y.; Altounian, Z.; Zhang, Q.; Ping Liu, J. First-Principles Survey on the Doping of Ga in $Nd_2Fe_{14}B$. *J. Appl. Phys.* **2014**, *115*, 17A702. [CrossRef]
30. Liu, X.B.; Nlebedim, I.C. Segregation of Al and Its Effect on Coercivity in Nd-Fe-B. *AIP Adv.* **2024**, *14*, 015030. [CrossRef]
31. Tatetsu, Y.; Tsuneyuki, S.; Gohda, Y. First-Principles Study on Substitution Effects in $Nd_2(Fe, X)_{14}B$. *Materialia* **2018**, *4*, 388–394. [CrossRef]
32. Girgis, K.; Kraft, M.; Weis, U.; Fischer, P.; Sostarich, M. Crystal and Magnetic Structure of the Permanent Magnet Materials $Nd_2Fe_{14-x}Co_xB$ (x = 0–14). *J. Less Common Met.* **1990**, *162*, 335–342. [CrossRef]
33. Fuerst, C.D.; Herbst, J.F.; Alson, E.A. Magnetic Properties of $Nd_2(Co_xFe_{1-x})_{14}B$ Alloys. *J. Magn. Magn. Mater.* **1986**, *54–57*, 567–569. [CrossRef]
34. Hu, B.P.; Li, H.S.; Gavigan, J.P.; Coey, J.M.D. Intrinsic Magnetic Properties of the Iron-Rich $ThMn_{12}$-Structure Alloys $R(Fe_{11}Ti)$; R=Y, Nd, Sm, Gd, Tb, Dy, Ho, Er, Tm and Lu. *J. Phys. Condens. Matter* **1989**, *1*, 755. [CrossRef]
35. Srinithi, A.K.; Sepehri-Amin, H.; Tang, X.; Tozman, P.; Li, J.; Zhang, J.; Kobayashi, S.; Ohkubo, T.; Nakamura, T.; Hono, K. Phase Relations and Extrinsic Magnetic Properties of Sm–(Fe,Co)–Ti–(Ga)-Based Alloys for ThMn12-Type Permanent Magnets. *J. Magn. Magn. Mater.* **2021**, *529*, 167866. [CrossRef]
36. Hirayama, Y.; Takahashi, Y.K.; Hirosawa, S.; Hono, K. Intrinsic Hard Magnetic Properties of $Sm(Fe_{1-x}Co_x)_{12}$ Compound with the ThMn12 Structure. *Scr. Mater.* **2017**, *138*, 62. [CrossRef]
37. Liu, X.B.; Ping Liu, J.; Zhang, Q.; Altounian, Z. The Fe Substitution in $Nd_2(Fe,M)_{14}B$ (M = Si, Ge and Sn): A First-Principles Study. *Comput. Mater. Sci.* **2014**, *85*, 186–192. [CrossRef]

38. Ozaki, T. Variationally Optimized Atomic Orbitals for Large-Scale Electronic Structures. *Phys. Rev. B* **2003**, *67*, 155108. [CrossRef]
39. Ozaki, T.; Kino, H. Numerical Atomic Basis Orbitals from H to Kr. *Phys. Rev. B* **2004**, *69*, 195113. [CrossRef]
40. Perdew, J.P.; Burke, K.; Ernzerhof, M. Generalized Gradient Approximation Made Simple. *Phys. Rev. Lett.* **1996**, *77*, 3865–3868. [CrossRef]
41. Richter, M. Band Structure Theory of Magnetism in 3d-4f Compounds. *J. Phys. D Appl. Phys.* **1998**, *31*, 1017–1048. [CrossRef]
42. Coey, J. *Magnetism and Magnetic Materials*; Cambridge University Press: Cambridge, UK, 2010.
43. Tolman, R.C. *The Principles of Statistical Mechanics*; Dover Pub. Inc.: New York, NY, USA, 1979.
44. Pashov, D.; Acharya, S.; Lambrecht, W.R.L.; Jackson, J.; Belashchenko, K.D.; Chantis, A.; Jamet, F.; van Schilfgaarde, M. Questaal: A Package of Electronic Structure Methods Based on the Linear Muffin-Tin Orbital Technique. *Comput. Phys. Commun.* **2020**, *249*, 107065. [CrossRef]
45. Andersen, O.K. Linear Methods in Band Theory. *Phys. Rev. B* **1975**, *12*, 3060–3083. [CrossRef]
46. Jepsen, O.; Andersen, O.K. The Electronic Structure of h.c.p. Ytterbium. *Solid State Commun.* **1971**, *9*, 1763–1767. [CrossRef]
47. Blöchl, P.E.; Jepsen, O.; Andersen, O.K. Improved Tetrahedron Method for Brillouin-Zone Integrations. *Phys. Rev. B* **1994**, *49*, 16223–16233. [CrossRef] [PubMed]
48. van Schilfgaarde, M.; Antropov, V.P. First-Principles Exchange Interactions in Fe, Ni, and Co. *J. Appl. Phys.* **1999**, *85*, 4827–4829. [CrossRef]
49. Matsuura, Y.; Hirosawa, S.; Yamamoto, H.; Fujimura, S.; Sagawa, M.; Osamura, K. Phase Diagram of the Nd-Fe-b Ternary System. *Jpn. J. Appl. Phys.* **1985**, *24*, 635–637. [CrossRef]
50. Koch, E.; Fischem, W. DIDO95 and VOID95—Programs for the Calculation of Dirichlet Domains and Coordination Polyhedra. *Z. Für Krist.-Cryst. Mater.* **1996**, *211*, 251–253. [CrossRef]
51. Kittel, C. *Introduction to Solid State Physics*, 8th ed.; John Wiley & Sons: Chicago, IL, USA, 2004.
52. Miedema, A.R. Energy Effects and Charge Transfer in Metal Physics; Modelling in Real Space. *Phys. B Condens. Matter* **1992**, *182*, 1–17. [CrossRef]
53. Momma, K.; Izumi, F. *VESTA 3* for Three-Dimensional Visualization of Crystal, Volumetric and Morphology Data. *J. Appl. Crystallogr.* **2011**, *44*, 1272–1276. [CrossRef]
54. Liu, X.B.; Altounian, Z. First-Principles Calculation on the Curie Temperature of GdFeSi. *J. Appl. Phys.* **2010**, *107*. [CrossRef]
55. Liu, X.B.; Altounian, Z. Magnetic Moments and Exchange Interaction in Sm(Co, Fe)$_5$ from First-Principles. *Comput. Mater. Sci.* **2011**, *50*, 841–846. [CrossRef]